A study of metal-bearing nanoparticles from the Kangjiawan Pb-Zn deposit and their prospecting significance

Xiang Liu[a,b,c], Jianjin Cao[a,b,c,*], Yingkui Li[a,b,c], Guai Hu[a,b,c], Guoqiang Wang[a,b,c]

[a] *School of Earth Sciences and Engineering, Sun Yat-sen University, Guangzhou 510275, China*
[b] *Guangdong Provincial Key Laboratory of Geological Processes and Mineral Resource Exploration, School of Earth Sciences and Engineering, Sun Yat-sen University, Guangzhou 510275, China*
[c] *Guangdong Provincial Key Laboratory of Geodynamics and Geohazards, School of Earth Sciences and Engineering, Sun Yat-sen University, Guangzhou 510275, China*

A B S T R A C T

Over the years, using novel methods to find deep-seated ore resources has always been a hot research topic. In this paper, we present a new method to investigate deep-seated orebodies by characterizing metal-bearing nanoparticles (e.g., morphological features and chemical compositions) in various media (deep/shallow groundwater, ascending gas flow, and soil) via transmission electron microscopy (TEM). From the Kangjiawan Pb-Zn deposit (the study area), the metal-bearing nanoparticles collected from different media contain similar contents of ore-forming elements (e.g., Cu, Zn, Pb, Fe and S) and are strongly related to the presence of deep-seated orebodies. These ore-related nanoparticles are grouped into four main categories: (i) amorphous, (ii) single-crystal, (iii) poly-crystal and (iv) complex poly-crystal. In particular, many amorphous nanoparticles in different media can transfer ore-forming elements and provide mineralization information. We propose that the ore-forming elements exist and migrate in the form of these four types of nanoparticles. The results can explain the geochemical anomalies and provide insights on the role of nanoparticles in post-mineralization ore-related elemental dispersion, and could be useful in exploration for concealed orebodies.

1. Introduction

To date, geophysical and geochemical explorations are common prospecting methods that play an important role in ore discovery. Geophysical exploration methods involve gravity prospecting, magnetic prospecting, electrical prospecting, etc. (Aina and Olorunfemi, 1996; Mohanty et al., 2011). For example, many abnormal areas were delineated around the Olympic Dam deposit in Southern Australia through studying regional gravity and magnetic anomaly data (Roberts and Hudson, 1983). Late-time transient electromagnetic methods were applied to discover and delineate the Cosmos nickel sulfides deposit in the Leinster area, Western Australia (Craven et al., 2000). Varentsov et al. (2013) used magnetotelluric methods to provide a number of prospective mining targets that were verified by subsequent drilling.

Geochemical exploration methods include mainly primary and secondary dispersion halos, stream sediment, MMI (Mobile Metal Ions), enzyme leaching, MOMEO (Leaching of Mobile Forms of Metal in Overburden), electrogeochemistry, biogeochemistry, geogas and hydrochemistry (Kristiansson and Malmqvist, 1982; Malmqvist and Kristiansson, 1985; Butt and Gole, 1985; Clark et al., 1990; Antropova et al., 1992; Wang et al., 1997; Mann et al., 1998; Luo et al., 1999; Williams et al., 2002; Kelley et al., 2003; Cameron et al., 2004; Anand et al., 2007; Ghavami-Riabi et al., 2008; Wang et al., 2008; Koplus et al., 2009; Leybourne and Cameron, 2010; Gao et al., 2011; Geffen et al., 2012; Noble et al., 2013; Park et al., 2014; Zhou et al., 2014; Yilmaz et al., 2015; Gray, 2016; Lintern and Anand, 2017; Wan et al., 2017). These methods are used to detect mineralization signatures and delineate geochemical anomalies areas to locate the orebodies. Nevertheless, previous studies are mainly dedicated to the elemental/ionic concentrations and the pH value of the samples (e.g., rock, sediments, mineral, water and gas). In addition to mineralization, a relatively high elemental content in the samples can be caused by some factors such as chemical and mechanical processes, and thus it is difficult to distinguish multi-source anomalies (Anand et al., 2016).

Using atomic force microscopy (AFM), scanning electron microscopy (SEM) and transmission electron microscopy (TEM), Tong et al. (1998) confirmed that the materials carried by ascending gas flow from the orebodies were in the form of nanoparticles. Cao et al. (2009a) identified gold nanoparticles and other Hg-, Zn-, Pb-, and W-bearing nanoparticles in the ascending gas flow in the Changkeng gold deposit,

and characterized the nanoparticles (category, size, shape, chemical component, and elemental combination) via TEM. Cao first proposed to use nanoparticles in ore prospecting (Cao et al., 2009a; Cao, 2009b). Subsequently, metal-bearing nanoparticles in ascending gas flow, groundwater, fault gouge, plant and invertebrate tissues were found in different deposits (Wei et al., 2013; Cao et al., 2015; Dai et al., 2015; Luo et al., 2015; Li et al., 2016; Wang et al., 2016; Hu et al., 2015, 2017, 2018; Cheng et al., 2018).

The Kangjiawan deposit is chosen as the study area here. The deposit, an important Pb-Zn producing area, is located in the southern margin of the Hengyang Basin (South China). The basin is with well-circulated groundwater, making groundwater samples readily available (Zhang et al., 2007; Zuo et al., 2014, 2016). In this paper, we aim to (a) characterize the nanoparticles sampled from various media; (b) elucidate the relationship between the metal-bearing nanoparticles and the deep-seated orebodies and (c) determine the forms of migration of the ore-forming elements.

2. Geological setting

The large Kangjiawan Pb-Zn sulfide deposit is situated in the northeastern part of the Shuikoushan orefield in Changning, Hunan Province (Fig. 1a). Tectonically, the orefield is close to the northwestern margin of the Cathaysia Block, in the western part of the Shi-Hang rift, and in the northern end of the Leiyang-Linwu fold belt (Zhang et al., 2007; Zuo et al., 2014). The exposed stratigraphy at the orefield is composed of Lower Permian marlstone and argillaceous limestone, Upper Permian shale and siltstone, and Triassic limestone. These rocks are unconformably overlain by Jurassic-Cretaceous sandstone and shale. A series of NS- to NNE-trending reverse faults and folds are well developed, and the major Fault 22 (F22) is ore-related (Zeng et al., 2000; Zhang et al., 2007). In the orefield, granitoids include the Shuikoushan granodiorite, Laomengshan dacite porphyry,

Xinmengshan rhyolite porphyry and Xianrenyan granodiorite porphyry (Zuo et al., 2014; Huang et al., 2015; Yang et al., 2016) (Fig. 1b).

The deposit is composed of 61 concealed orebodies that are closely related to the silicified breccias (Xu et al., 2002; Zuo et al., 2016). The orebodies can be grouped into seven ore clusters: five in the silicified breccia zones, which are located in or near the unconformity between the Jurassic and Permian rocks, and the other two occur in the Lower Permian argillaceous limestone. The orebodies are mainly stratiform or lenticular (Zeng et al., 2000; Zuo et al., 2014, 2016). Metallic minerals are mainly galena, sphalerite and pyrite, followed by chalcopyrite, pyrrhotine, hematite, arsenopyrite, bornite, native gold, native silver and silver sulfosalts. Silver minerals (electrum, freibergite, pearceite and pyrargyrite) at the micrometer scale incorporated in hypogene ores were detected by Zeng et al. (2000). Non-metallic minerals include predominantly quartz and calcite, with minor chalcedony, fluorite and barite (Zeng et al., 2000; Zhao et al., 2014). Major alteration styles include silicic, carbonate and chlorite, plus skarn and hornfels in southern Kangjiawan (Zeng et al., 2000).

There are three aquifers at Kangjiawan: Aquifer I is distributed along the overturned anticline in the Cretaceous sequence above the orebodies, and drains into the Kangjia creek and low-lying area. Supplied by meteoric water, it is a highly fractured aquifer with abundant water content (1.0–3.7 L/s.m). Aquifer II is a N-S trending karstic-fissured aquifer, and occurs in the silicified breccias in direct contact with the orebodies. It is mainly supplied by peripheral deep-water circulation, and minor by Aquifer III. The fractured Aquifer III contains low water content, and occurs in the Jurassic sequence in the middle and eastern Kangjiawan. The aquifer is supplied by meteoric water that seeps through cracks of weathered rocks (Hunan Nonferrous Team 217, 1982).
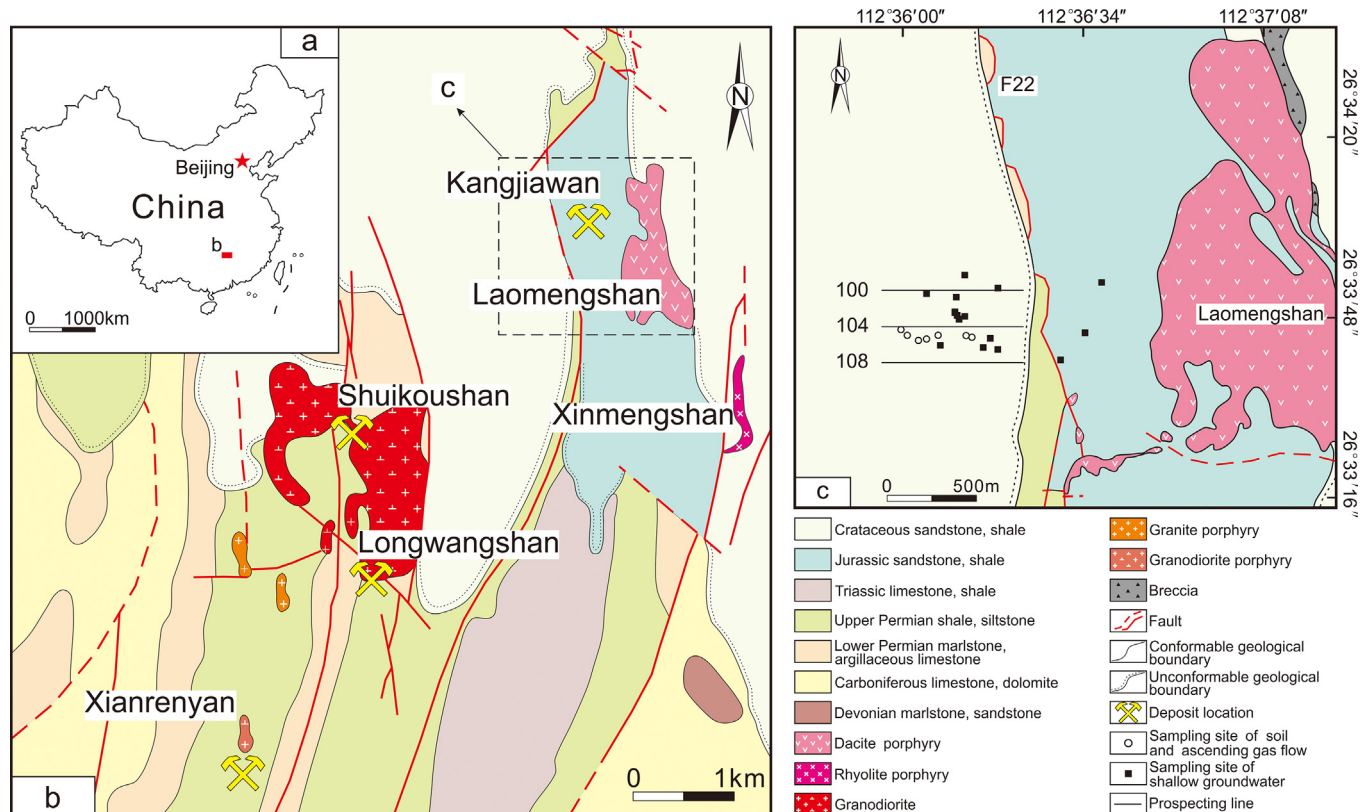

Fig. 1. (a) Location of the study area in China. (b) Sketch map of the Shuikoushan orefield (modified from Yang, 1985). (c) Sketch map of the Kangjiawan deposit (modified from the unpublished map provided by Hunan Shuikoushan Nonferrous Metals Group).

3. Sampling and analytical methods

3.1. Sampling location and methods

To avoid mining-related contamination, our sampling focused on southern Kangjiawan where proven but unexploited deep-lying orebodies are located. The collected samples include (i) deep groundwater, (ii) shallow groundwater, (iii) ascending gas flow, and (iv) soil. We used 500 ml wide-mouthed polyethylene bottles for collecting groundwater samples. After washing three times with ultrapure water, the bottles were dried in pollution-free conditions. The sampling method was performed as follows: deep groundwater samples were collected in the No. 12 and No. 13 levels (at −350 m and below) near the undistributed orebodies close to Aquifer II. Each bottle was placed below the position with well-developed fissure water, and a water sample (200 to 400 ml) from the rock fissure was collected. To avoid contamination, deep groundwater seeping from the fissure was dripped straight into the bottles. The pH of the samples was measured on site and range from 4.68 to 7.20. The shallow groundwater samples were collected through water pumps or wells, using the 500 ml wide-mouthed polyethylene bottles. The sampling sites were mainly located between Prospecting Lines No. 100 and No. 108, distal from big cities or industrial centers (Fig. 1c). To avoid external affections, the samples were collected after discharging the water for over three minutes. The sampling depth ranged from 2 to 50 m, and the pH values ranged from 5.36 to 7.05. Background water samples were collected at the Baitudabu village (Gaoyao, Guangdong), which is located in the Baitu Basin and has similar geological conditions to the Hengyang Basin (e.g., stratigraphy, structure, and hydrogeological setting). Additionally, the background sampling sites were unaffected by mining, and share similar sampling depth, rock type and pH value with the shallow groundwater sampling sites. The water samples were collected through water pumps or wells from 8 to 20 m deep, using also 500 ml wide-mouthed polyethylene bottles. Finally, all the bottles were sealed, labelled, and stored under room temperature.

Samples of ascending gas flow and soil were collected along Prospecting Line No. 104 (Fig. 1c). A sampling device for collecting ascending gas flow samples was similar to those used in Cao et al. (2015) and Luo et al. (2015): A carbon-coated nickel TEM grid was fixed to the end of a funnel spout with a silica gel plug, a small plastic tube, rubber bands and two nylon nets. These materials were washed twice with ultra-pure water before assembling. The whole set-up was protected from contamination by using a polyvinyl chloride (PVC) pipe and a cup. After burying the device in a hole (60–80 cm deep), a plastic film was placed on the surface as a rain shield. The TEM grids were retrieved after 60 days. Clean tweezers were used to pick up the TEM grids, then the grids with the attached nanoparticles were placed in a clean and dry sample box. For soil sampling, around 50 g sample from 50 cm below ground was collected from each sampling site, using a shovel and a clean sampling bag. After sealing and labelling, the soil samples and the carbon-coated nickel TEM grids with attached nanoparticles were stored in a dry place.

3.2. Analytical methods

Deep and shallow groundwater samples were preprocessed under clean bench conditions, following the procedures described in Li et al. (2016) and Cheng et al. (2018). Light shaking of the bottles at the outset was performed to eliminate the uneven dispersion of nanoparticles in aqueous solutions induced by gravitational settling. After that, a pipette was used to transfer the collected water sample onto a carbon-coated nickel TEM grid, and a new pipette was used for each water sample. Only a small amount of solution was allowed to be transferred each time, and the procedure was repeated 4 to 5 times. The soil samples were prepared in the way described by Wang et al. (2016). After being dried and screened through a mesh (size 80), the soil samples were placed in a beaker. A TEM grid was suspended inside the beaker with tweezers enabling adsorption of the freely settled soil nanoparticles. Then, the TEM grids were placed into a clean and dry sample box.

After preprocessing, the nanoparticles deposited on the TEM grids, were analyzed by transmission electron microscopy (TEM, Tecnai G2F30S-Twin, America) at the Yangzhou University Testing Center and the Lanzhou University Testing Center. The specific parameters of the test instruments were as follows: the maximum accelerating voltage was 300 kV, the dot resolution was 0.20 nm, the linear resolution was 0.102 nm, the resolution of STEM HAADF was 0.17 nm, and the maximum magnification of the TEM and STEM was 1 million and 2.3 million times, irrespectively. The morphological features, energy dispersive X-ray spectra (EDS), high-resolution transmission electron microscopy (HRTEM) image, and selected area electron diffraction (SAED) pattern of the nanoparticles were obtained. Carbon and Ni contents were not considered due to the high background caused by the carbon-coated nickel TEM grid.

4. Results

4.1. Results from the deposit

Metal-bearing nanoparticles were identified and analyzed in the samples of deep groundwater (n = 36), shallow groundwater (n = 72), ascending gas flow (n = 29), and soil (n = 33). Mineralization-related elements were commonly detected in nanoparticles, including Pb, Zn, Cu and Fe, which usually appeared along with S. A small proportion of the nanoparticles containing common elements (e.g., O, Na, K, Si and Ba) were also found. They were commonly excluded from the metal-bearing nanoparticles because of the relatively low contrast under the TEM imaging. It is noted that the metal-bearing nanoparticles from the different media exhibit distinct diversity in crystal/aggregate features, which are described in the following section.

4.1.1. Characteristics of amorphous nanoparticles

Amorphous metal-bearing nanoparticles are abundant in the samples of various media (Table 1). An Fe-Zn-S-O-bearing nanoparticle (ID: 1) is found in a deep groundwater sample. It is irregularly shaped and

Table 1
Information about amorphous nanoparticles from the deposit.

Particle ID	Sampling media	Size (nm)	Shape	Crystallinity	Element									
						O	Al	Si	Ca	S	K	Fe	Cu	Zn	P
1	deep groundwater	300 × 500	irregular	amorphous	wt%	64.03				10.67	0.85	19.78		3.32	1.30
					at%	83.29				6.93	0.45	7.37		1.05	0.87
2	shallow groundwater	unmeasurable	irregular granular aggregation	amorphous	wt%	41.39	4.25	9.52	1.55			28.14	15.12		
					at%	66.94	4.08	8.77	1.00			13.03	6.15		
3	ascending gas flow	100 × 200	irregular	amorphous	wt%	26.18		2.63		16.96	1.01		53.20		
					at%	52.40		3.00		16.95	0.83		26.81		
4	soil	200 × 300	hexagonal	amorphous	wt%	45.48	3.81	7.01				29.32	14.36		
					at%	71.33	3.54	6.27				13.17	5.67		

Fig. 2. An amorphous Zn-Fe-S-O-bearing nanoparticle in deep groundwater samples: (a) TEM image; (b) SAED pattern. An amorphous Fe-Cu-Si-Al-Ca-O-bearing nanoparticle aggregation in shallow groundwater samples: (c) TEM image; (d) SAED pattern. An amorphous Cu-S-O-bearing nanoparticle in ascending gas flow samples: (e) TEM image; (f) SAED pattern. An amorphous Cu-Fe-Si-Al-O-bearing nanoparticle in soil samples: (g) TEM image; (h) SAED pattern.

Table 2
Information about single-crystal nanoparticles from the deposit.

Particle ID		Sampling media	Size (nm)	Shape	Crystallinity	Element										
							O	Na	Mg	S	Cl	Fe	Cu	Zn	Ag	Mo
5	I	shallow groundwater	unmeasurable	irregular granular aggregation	single-crystal	wt%				1.14	1.48		2.50		94.86	
						at%				3.57	4.19		3.96		88.26	
	II		unmeasurable	rounded granular aggregation	poly-crystal	wt%	33.71	11.91	0.98	2.23		7.46	10.04	15.31		18.33
						at%	61.03	15.00	1.17	2.01		3.86	4.57	6.78		5.53
6		shallow groundwater	200 × 200	rounded	single-crystal	wt%	33.95					66.04				
						at%	64.21					35.78				
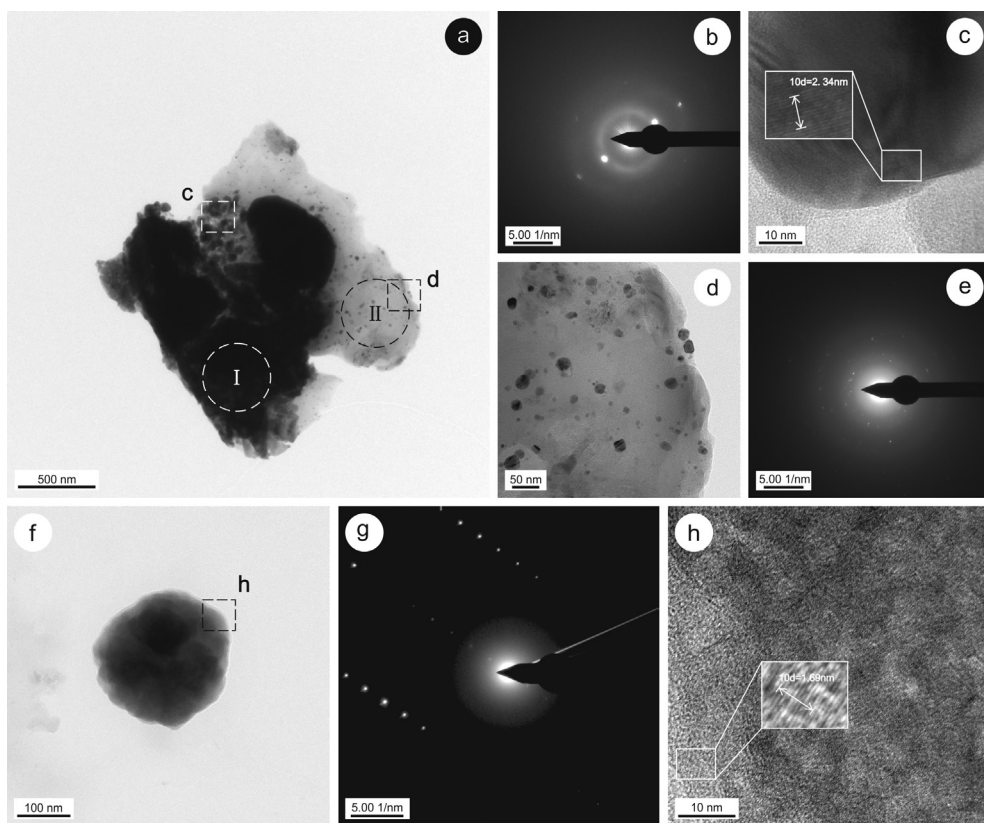
Fig. 3. Single-crystal Ag nanoparticles and crystalline Mo-Zn-Cu-Fe-Na-S-O-bearing nanoparticles in shallow groundwater samples: (a) TEM image; (b) SAED pattern of the single-crystal Ag nanoparticles marked as circle I in a; (c) HRTEM image obtained from the white rectangle in a; (d) detailed image obtained from the black rectangle in a; (e) SAED pattern of the poly-crystal Mo-Zn-Cu-Fe-Na-S-O-bearing nanoparticles marked as circle II in a. A single-crystal Fe_2O_3 nanoparticle in shallow groundwater samples: (f) TEM image; (g) SAED pattern; (h) HRTEM image obtained from the black rectangle in f.
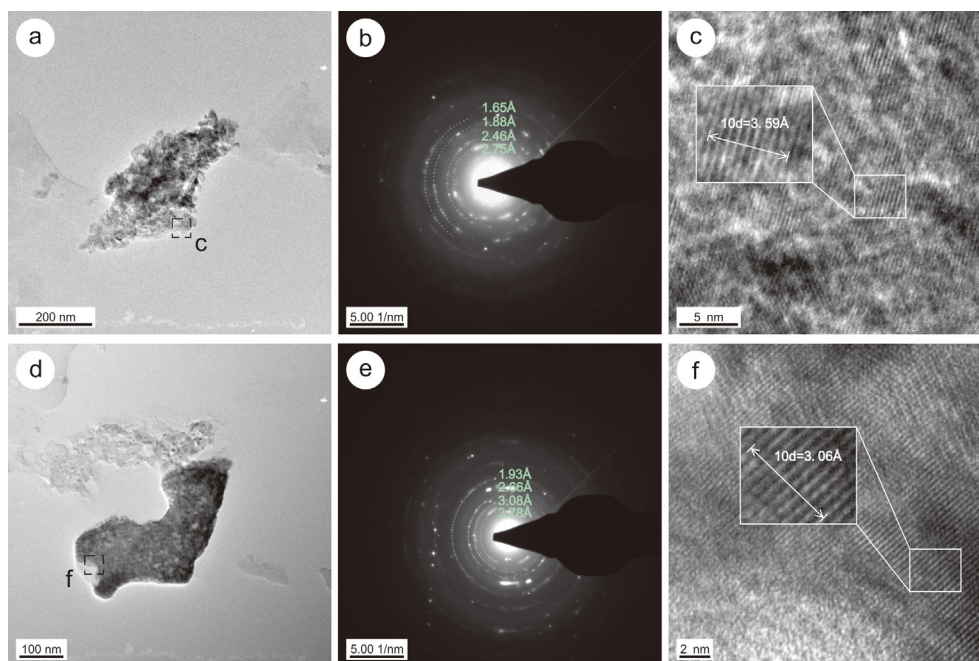
Table 3
Information about poly-crystal nanoparticles from the deposit.

Particle ID	Sampling media	Size (nm)	Shape	Crystallinity	Element		O	F	Na	Al	Si	S	Cl	K	Ca	Mn	Fe	Co	Cu	Zn	Pb	Os
7	shallow groundwater	unmeasurable	cubic granular aggregation	poly-crystal	wt%		7.12								0.41		0.58		91.87			
					at%		23.30								0.54		0.54		75.61			
8	shallow groundwater	unmeasurable	irregular granular aggregation	poly-crystal	wt%		16.40	6.82				0.64	0.07	0.76	3.10		53.89		18.28			
					at%		37.19	13.03				0.73	0.07	0.70	2.81		35.00		10.43			
9	deep groundwater	unmeasurable	nearly rounded granular aggregation	poly-crystal	wt%		31.80	5.45	8.81		0.02		0.82		0.98	23.27	1.40	1.12		26.28		
					at%		55.57	8.02	10.71		0.02		0.65		0.68	11.84	0.70	0.53		11.24		
10	soil	unmeasurable	nearly rounded granular aggregation	poly-crystal	wt%		30.61			3.03	3.13						53.34					
					at%		60.84			3.57	3.55						30.37					
11	ascending gas flow	100 × 400	irregular	poly-crystal	wt%		14.14				1.24	11.12			2.75				8.47		62.25	9.87
					at%		49.72				2.49	19.51			3.86				7.49		16.89	1.65

Fig. 4. Poly-crystal Cu_2O nanoparticles in shallow groundwater samples: (a) TEM image; (b) SAED pattern. Poly-crystal Fe_3O_4 nanoparticles in shallow groundwater samples: (c) TEM image; (d) SAED pattern. Poly-crystal Zn-Mn oxide nanoparticles in deep groundwater samples: (e) TEM image; (f) SAED pattern.

300 × 500 nm in size (Fig. 2a). With broad amorphous diffraction rings in the SAED pattern (Fig. 2b), this nanoparticle is amorphous. Meanwhile, an Fe-Cu-Si-Al-Ca-O-bearing nanoparticle aggregation (ID: 2) is found in a shallow groundwater sample (Fig. 2c, d), which is also amorphous.

In an ascending gas flow sample, an irregular nanoparticle (ID: 3) is found containing Cu (53.20%), S (16.96%), O (26.18%), Si (2.63%) and K (1.01%) (Fig. 2e). With broad amorphous diffraction rings in the SAED pattern (Fig. 2f), this nanoparticle is amorphous. Thus, it may be a Cu-S-O-bearing nanoparticle with a trace amount of Si and K. In a soil sample, a hexagonal (size: 200 × 300 nm) Cu-Fe-Si-Al-O-bearing nanoparticle (ID: 4) is found (Fig. 2g). None of the diffraction spots are shown in the SAED pattern (Fig. 2h).

4.1.2. Characteristics of single-crystal nanoparticles

Single-crystal nanoparticles are rarely observed, and their EDS results are listed in Table 2. Notably, Ag has been detected in the nanoparticle aggregations (ID: 5; Fig. 3a). Among them, the nanoparticle aggregation with high contrast under the TEM imaging (ID: 5I) contains Ag (94.86%), Cu (2.50%), Cl (1.48%) and S (1.14%), and it is with a single-crystal pattern (Fig. 3b). The HRTEM image (Fig. 3c) reveals that one of its d-spacings is 2.34 Å, which matches with that of the (1 1 1) plane of the Ag sample (PDF# 04-0783). Fig. 3d illustrates that a Mo-Zn-Cu-Fe-Na-S-O-bearing nanoparticle aggregation (ID: 5II) with scattered diffraction spots in the SAED pattern (Fig. 3e), indicative of a

Fig. 5. Poly-crystal Fe_2O_3 nanoparticles in soil samples: (a) TEM image; (b) SAED pattern; (c) HRTEM image obtained from the rectangle in a. A poly-crystal $PbSO_4$ nanoparticle in ascending gas flow samples: (d) TEM image; (e) SAED pattern; (f) HRTEM image obtained from the rectangle in d.

Table 4
Information about complex poly-crystal nanoparticles from the deposit.

Particle ID		Sampling media	Size (nm)	Shape	Crystallinity	Element								
							O	Si	S	Ca	Cu	Pb	As	Bi
12		deep groundwater	unmeasurable	nearly rounded granular aggregation	complex poly-crystal	wt%	13.89		8.31	4.22	53.42	20.14		
						at%	39.99		11.94	4.85	38.72	4.47		
13		ascending gas flow	unmeasurable	irregular granular aggregation	complex poly-crystal	wt%	5.78		3.69		45.85	39.14	5.53	
						at%	24.73		7.88		49.39	12.93	5.05	
14	I	ascending gas flow	150 × 150	cubic	complex poly-crystal	wt%	10.94		9.82		7.41	71.80		
						at%	47.06		21.08		8.02	23.83		
	II		unmeasurable	rounded granular aggregation		wt%	9.30	1.20			12.90	42.82	13.41	20.35
						at%	44.37	3.26			15.49	15.77	13.65	7.43

crystalline nature. Another rounded Fe-O-bearing nanoparticle (ID: 6; Fig. 3f) is found with the Fe:O atomic ratio of nearly 2:3. Regularly distributed diffraction spots are shown in the SAED pattern (Fig. 3g), indicative of a single-crystal nature. The HRTEM image (Fig. 3h) reveals that one of the d-spacings is 1.69 Å, which matches that of the (1 1 6) plane of the Fe_2O_3 sample (PDF# 33-0664).

4.1.3. Characteristics of poly-crystal nanoparticles
Poly-crystal nanoparticles are commonly observed in this study. They appear as individual particles or as particle aggregations. The EDS results are shown in Table 3. In a shallow groundwater sample, a cubic nanoparticle aggregation (ID: 7; Fig. 4a) is found to contain Cu (91.87%), O (7.12%), Fe (0.58%) and Ca (0.41%). The SAED pattern (Fig. 4b) reveals that the nanoparticle aggregation is polycrystalline, and the d-spacings are calculated to be 1.32 Å, 1.55 Å, 2.19 Å, 2.52 Å and 3.08 Å. These calculated d-spacings are well matched with those of the Cu_2O sample (PDF# 75–1531). Fig. 4c shows a nanoparticle aggregation (ID: 8) that contains Fe (53.89%), Cu (18.28%), F (6.82%), and O (16.40%). The Fe:O atomic ratio is nearly 3:4. Several diffraction rings are clearly shown in the SAED pattern (Fig. 4d), and the d-spacings are calculated to be 1.01 Å, 1.18 Å, 1.45 Å, 2.05 Å and 2.49 Å. Compared with the Fe_3O_4 sample (PDF# 72–2303), the nanoparticle aggregation can be a magnetite with a trace amount of Cu, F, and Ca. In a deep groundwater sample, a nanoparticle aggregation (ID: 9; Fig. 4e)

contains Zn (26.28%), Mn (23.27%), O (31.80%), Na (8.81%) and F (5.45%). The SAED pattern (Fig. 4f) shows that it is polycrystalline, and the calculated d-spacings are 1.52 Å, 2.50 Å and 3.02 Å. They match well with those of the $ZnMn_2O_4$ sample (PDF# 24–1133). In a soil sample, a nanoparticle aggregation (ID: 10; Fig. 5a) contains Fe, O, Si and Os. Regular diffraction rings are shown, and the d-spacings are calculated to be 1.65 Å, 1.88 Å, 2.46 Å and 2.75 (Fig. 5b). The HRTEM image (Fig. 5c) reveals that one of the crystalline interplanar spacings is nearly 3.59 Å. After comparing with the Fe_2O_3 sample (PDF# 33–0664), the nanoparticles can be classified as Fe oxides with a small amount of Os, Si and Al. In an ascending gas flow sample, an irregular polycrystalline Pb-Cu-S-Ca-Si-O-bearing nanoparticle (ID: 11; Fig. 5d) is found with its calculated d-spacings to be 1.93 Å, 2.66 Å, 3.08 Å and 3.78 Å (Fig. 5e). As shown in Fig. 5f, one of the d-spacings is measured as 3.06 Å. Thus, this nanoparticle resembles the $PbSO_4$ sample (PDF# 36–1461) with a trace amount of Cu, Ca and Si.
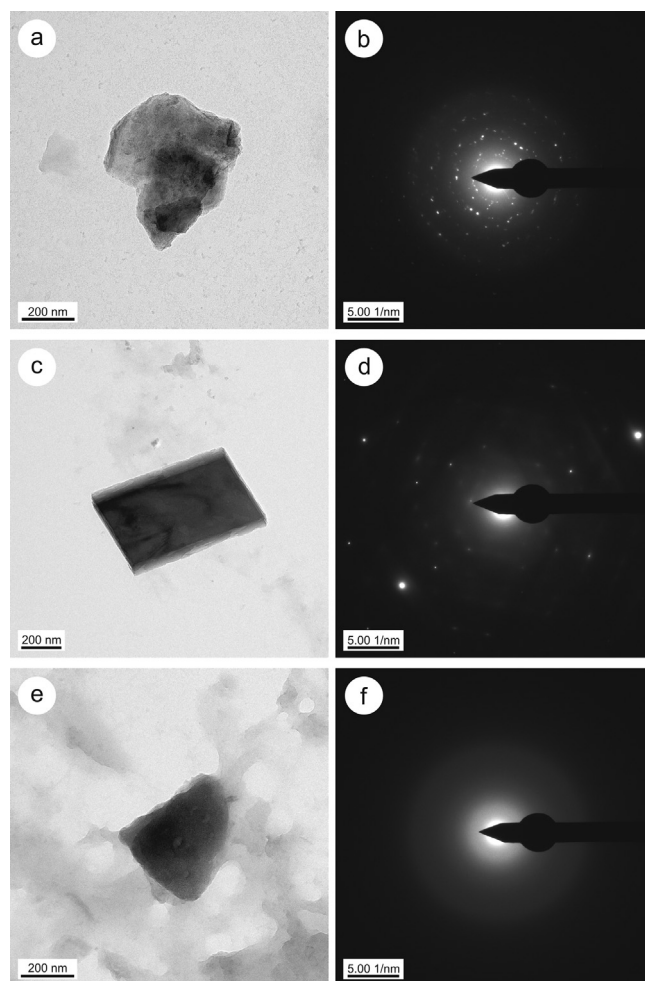
4.1.4. Characteristics of complex poly-crystal nanoparticles
This kind of polycrystalline nanoparticle aggregation is featured by its diverse nanoparticles with different morphologies and chemical components (Table 4). Fig. 6a presents a nanoparticle aggregation (ID: 12) observed in a deep groundwater sample. It contains Cu, Pb, S, O and Ca. Intricate diffraction rings are shown in the SAED pattern (Fig. 6b). In an ascending gas flow sample, a nanoparticle aggregation (ID: 13;
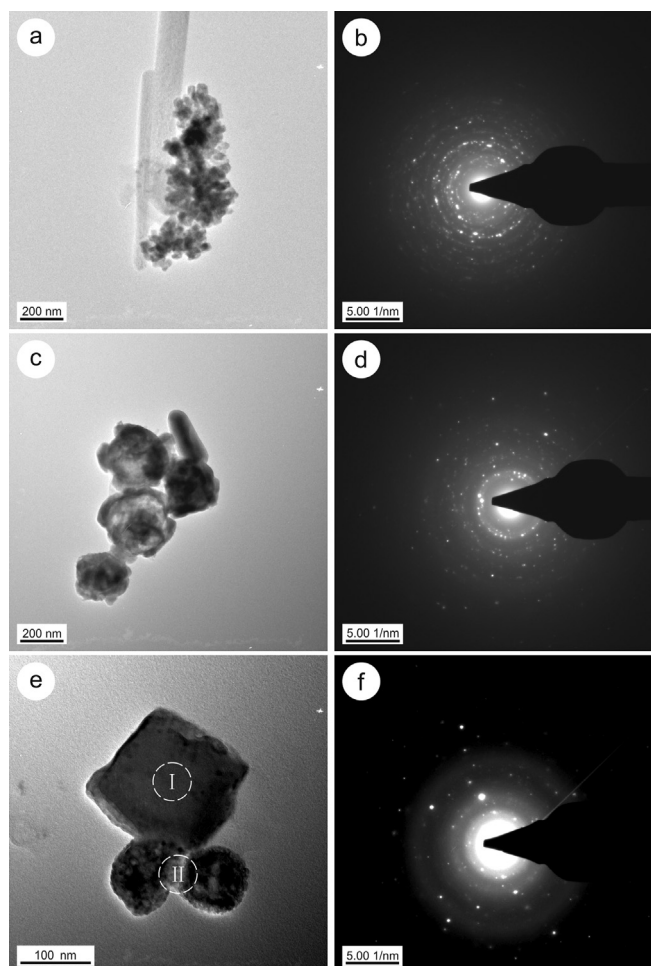
Fig. 6. Complex poly-crystal Cu-Pb-S-Ca-O-bearing nanoparticles in deep groundwater samples: (a) TEM image; (b) SAED pattern. Complex poly-crystal Cu-Pb-As-S-O-bearing nanoparticles in ascending gas flow samples: (c) TEM image; (d) SAED pattern. Complex poly-crystal aggregation composed of a cubic Pb-Cu-S-O-bearing nanoparticle and rounded Pb-Cu-As-Bi-Si-O-bearing nanoparticles in ascending gas flow samples: (e) TEM image; (f) SAED pattern.

Fig. 7. A complex poly-crystal Si-Al-K-Fe-O-bearing nanoparticle aggregation: (a) TEM image; (b) SAED pattern. A poly-crystal $CaCO_3$ nanoparticle: (c) TEM image; (d) SAED pattern. An amorphous silicon oxide nanoparticle: (e) TEM image; (f) SAED pattern.

Fig. 6c) contains Cu, Pb, As, S and O. The SAED pattern (Fig. 6d) reveals scattered diffraction spots. A typical complex poly-crystal nanoparticle aggregation (ID: 14), found in an ascending gas flow sample, is displayed in Fig. 6e. The aggregation consists of a cubic Pb-Cu-S-O-bearing nanoparticle (ID: 14I) with a size of 150×150 nm and two nearly rounded Pb-Cu-As-Bi-Si-O-bearing nanoparticles (ID: 14II). Due to the irregularly distributed diffraction spots, it is difficult to differentiate each nanoparticle according to the SAED pattern (Fig. 6f).

4.2. Results from background samples

In background water samples, more than 14 nanoparticles were tested, mainly including Ca-, Si-, Fe-, Al-, Ti-, and Ba-bearing nanoparticles. The nanoparticles, in contrast, have much simpler elemental combinations, and the materials from deep-seated orebodies disappeared in the background area. Table 5 shows the detailed EDS results of the representative nanoparticles. There is a Si-Al-K-Fe-O-bearing nanoparticle aggregation (ID: 15), which is observed in Fig. 7a. The SAED pattern (Fig. 7b) reveals scattered diffraction spots. Fig. 7c presents a quadrilateral Ca-O-bearing polycrystalline nanoparticle (ID: 16; Fig. 7d). The Ca to O atomic ratio is nearly 1:3, and the nanoparticle is inferred to be $CaCO_3$. Fig. 7e shows a regular Si-O-bearing amorphous

Table 5
Information about nanoparticles from background water.

Particle ID	Size (nm)	Shape	Crystallinity	Element		O	F	Na	Mg	Al	Si	S	K	Ca	Fe	Co
15	unmeasurable	irregular granular aggregation	complex poly-crystal		wt%	71.52			0.10	10.60	6.31		5.62	0.69	5.12	
					at%	83.62			0.08	7.35	4.20		2.68	0.32	1.71	
16	400 × 600	quadrilateral	poly-crystal		wt%	52.29	4.06	0.95				0.33		42.35		
					at%	71.19	4.65	0.90				0.22		23.01		
17	200 × 400	regular	amorphous		wt%	83.14		1.33	0.40	0.31	12.71			0.38	0.70	0.99
					at%	89.98		1.00	0.28	0.20	7.84			0.16	0.21	0.29
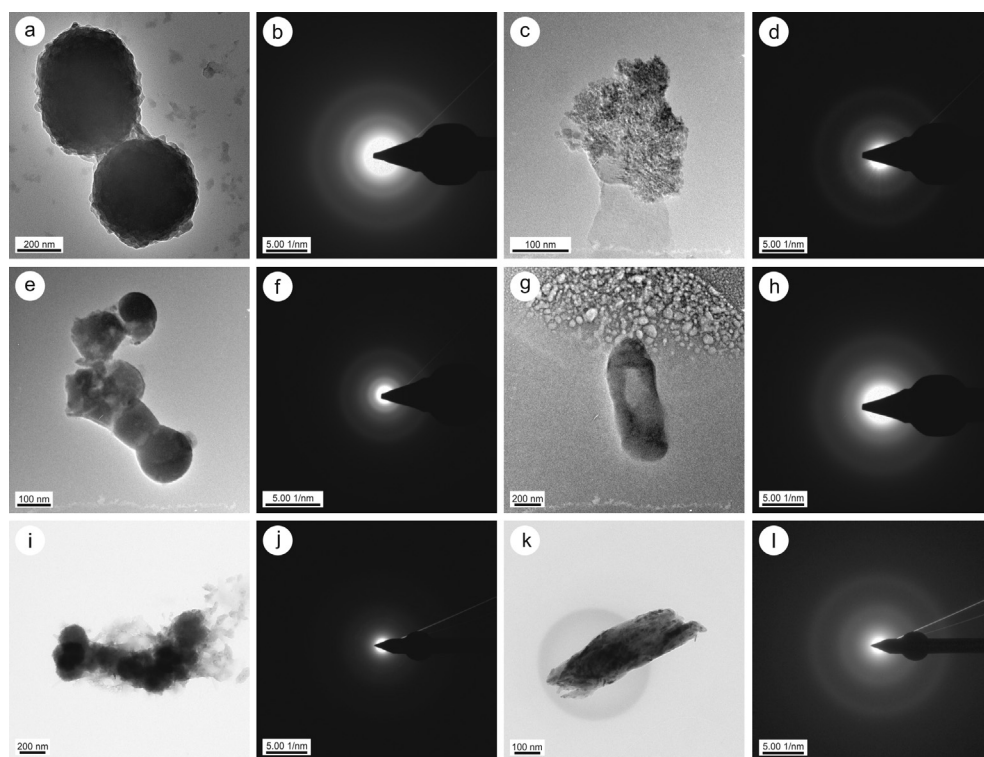
Fig. 8. An amorphous Cu-Ca-O-bearing nanoparticle aggregation: (a) TEM image; (b) SAED pattern. An amorphous Cu-Pb-Si-Al-O-bearing nanoparticle: (c) TEM image; (d) SAED pattern. An amorphous Cu-As-Sb-Pb-O-bearing nanoparticle aggregation: (e) TEM image; (f) SAED pattern. An amorphous Cu-Zn-Fe-S-O-bearing nanoparticle: (g) TEM image; (h) SAED pattern. An amorphous Fe-Zn-Ca-Na-O-bearing nanoparticle aggregation: (i) TEM image; (j) SAED pattern. An amorphous Pt-Co-Fe-Mn-Al-F-O-bearing nanoparticle: (k) TEM image; (l) SAED pattern.

nanoparticle (ID: 17; Fig. 7f), which consists dominantly of silicon oxide.

5. Discussion and conclusions

5.1. Classification of metal-bearing nanoparticles

Our TEM analysis results indicate that ore-forming elements can occur in the form of nanoparticles in various media (e.g., water, soil) around the deposit. The detected metal-bearing nanoparticles fall into four groups, i.e., amorphous, single-crystal, poly-crystal and complex poly-crystal. SAED patterns reveal that amorphous metal-bearing nanoparticles are common with broad amorphous diffraction rings. In contrast, single-crystal metal-bearing nanoparticles are less common than other types of nanoparticles, such as those containing Ag-Cu and Fe-O (Fig. 3a, f). They are characterized by regularly distributed diffraction spots shown in the SAED pattern.

Poly-crystal nanoparticles are found in diverse media, and occur as individual particles or particle aggregations. The aggregation consists of nanoparticles that are similar in size, shape and chemical components. Meanwhile, regularly distributed diffraction rings are distinct in the SAED pattern. Diverse elemental combinations, including Cu-S, Cu-Fe, Cu-Zn-Fe, Pb-Sb, Cu-Pb-As, Cu-Pb, Zn-Mn, Zn-Fe and Fe-Mn, are detected in the simple polycrystalline nanoparticle aggregation. On the contrary, the complex polycrystalline nanoparticle aggregation is usually composed of inhomogeneous materials; as such, SAED patterns reveal scattered diffraction spots or intricate diffraction rings, and EDS results show diverse types of metal contents. It is hard to differentiate each nanoparticle based on those SAED patterns and EDS results. Meanwhile, more complex elemental combinations are detected in the complex polycrystalline nanoparticle aggregation, including Pb-Cu-S, Pb-Cu-S-Ca, Pb-Cu-As-S, Pb-Sb-Cu, and Pb-Cu-As-Bi.

5.2. Significance of amorphous nanoparticles in ore-forming elements transport

Amorphous metal-bearing nanoparticles are commonly found in our groundwater, ascending gas flow and soil samples. They are regular, rounded, nearly quadrilateral or hexagonal; indications are that amorphous structures are irrelevant to the mature morphology (Pouget et al, 2010). Amorphous materials are not only consistent with parental minerals in chemical compositions but also have the ability to release significant amounts of metals (Consani et al., 2017; Konrad-Schmolke et al., 2018). In this respect, our attention is attracted to numerous amorphous metal-bearing nanoparticles in different media.

Our analysis suggested that amorphous nanoparticles commonly contain high and diverse types of metal contents (Fig. 8), including Cu, Cu-Pb, Cu-Pb-Sb-As, Cu-Zn-Fe-S, Fe-Zn and Fe-Co-Pt (Table 6). These nanoparticles can occur as particle aggregations (ID: 18, 20, 22; Fig. 8a, e, i) or individual particles (ID: 19, 21, 23; Fig. 8c, g, k). Their SAED patterns (Fig. 8b, d, f, h, j, l) reveal broad amorphous diffraction rings, suggesting the amorphous features. We observe that amorphous nanoparticles with different shapes and sizes can efficiently provide mineralization information. Different from the crystalline nanoparticles, the amorphous nanoparticles may have played a vital role in transporting a wide variety of ore-forming elements.

5.3. Comparison of metal-bearing nanoparticles from various media

Despite there are many types of metal-bearing nanoparticles, just a few single-crystal nanoparticles are observed in the shallow groundwater samples. Regarding the ore-related chemical components, the metal-bearing nanoparticles collected in the deep and shallow groundwater samples (commonly oxides or sulfates) contain mainly Cu, Zn, Fe and S, but rare Pb. Additionally, several Ag-, Sn-, Sb-, Mo-, and Ce-bearing nanoparticles are also found in the shallow groundwater samples. This suggests that the nanoparticles captured in the deep and shallow groundwater samples are highly similar.

Metal-bearing nanoparticles with different crystalline features and aggregated characteristics, except for single-crystal ones, are also found in both ascending gas flow and soil samples. In terms of ore-related elements, nanoparticles in the ascending gas flow samples (commonly oxides or sulfates) contain mainly Pb, Cu, Fe, S and As, and minor Zn, Sb, and Bi. Nanoparticles in the soil samples (commonly oxides) contain
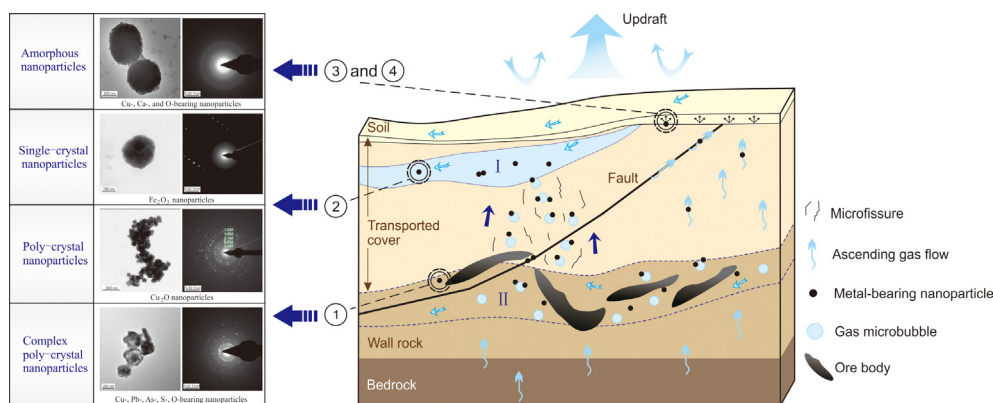
Table 6
Information about the amorphous nanoparticles related to ore-forming elements transport.

Particle ID	Ore-forming elemental combination	Sampling media	Size (nm)	Shape	Crystallinity	Element		O	F	Na	Mg	Al	Si	S	K	Ca	Mn	Fe	Co	Cu	Zn	Pb	Sb	As	P	Pt
18	Cu	ascending gas flow	unmeasurable	rounded granular aggregation	amorphous		wt%	5.84								3.31				90.83						
							at%	19.47								4.40				76.12						
19	Cu-Pb	ascending gas flow	120 × 200	irregular	amorphous		wt%	19.73				2.35	3.68				0.28			60.22		13.71				
							at%	44.80				3.17	4.76				0.25			39.16		7.84				
20	Cu-Pb-Sb-As	ascending gas flow	unmeasurable	nearly rounded granular aggregation	amorphous		wt%	15.25		0.25			1.01		1.79					17.98		35.23	14.59	13.87		
							at%	52.83		0.61			1.99		2.54					15.68		9.42	6.64	10.26		
21	Cu-Zn-Fe-S	deep groundwater	200 × 800	ellipsoidal	amorphous		wt%	36.82		7.29	2.58	1.51	1.73	15.94				6.22		15.32	11.12				1.42	
							at%	58.87		8.11	2.71	1.43	1.57	12.72				2.85		6.16	4.35				1.17	
22	Fe-Zn	deep groundwater	unmeasurable	nearly rounded granular aggregation	amorphous		wt%	32.53		5.09	1.21		0.56	1.03	0.60	5.58		48.51			4.84					
							at%	58.85		6.41	1.44		0.57	0.93	0.45	4.03		25.14			2.14					
23	Fe-Co-Pt	shallow groundwater	150 × 500	rod-like	amorphous		wt%	14.11	10.03			1.36	0.32		0.98	1.67	2.03	18.54	20.43							30.50
							at%	36.57	21.90			2.09	0.47		1.04	1.73	1.53	13.77	14.38							6.48

Table 7
Comparison of the nanoparticles in ascending gas flow and groundwater from the deposit.

Sampling media	Characteristics of the nanoparticles				
	Type	Ore-forming elemental combination	Size (nm)	Shape	Crystallinity
ascending gas flow	individual particle particle aggregation	Cu-S, Pb-Cu-S, Cu-Pb Pb-Cu-As-S, Cu-Pb-Sb-As, Pb-Cu-As-Bi-S	100 × 200-100 × 400 unmeasurable	irregular irregular granular aggregation, rounded granular aggregation, nearly rounded granular aggregation, cubic and rounded granular aggregation	amorphous, poly-crystal amorphous, complex poly-crystal
groundwater	individual particle particle aggregation	Cu-Zn-Fe-S, Fe-Co-Pt, Fe-Zn-S Fe-Zn, Pb-Cu-S, Cu-Fe, Zn-Mn, Ag-Cu-S, Mo-Zn-Cu-Fe-S	200 × 200-200 × 800 unmeasurable	irregular, rod-like, rounded, ellipsoidal irregular granular aggregation, rounded granular aggregation, cubic granular aggregation, nearly rounded granular aggregation	amorphous, single-crystal amorphous, single-crystal, poly-crystal, complex poly-crystal

Fig. 9. Schematic diagram of the ore-bearing nanoparticles formation and transport at Kangjiawan. ①-nanoparticles in deep groundwater; ②-nanoparticles in shallow groundwater; ③ and ④-nanoparticles in ascending gas flow and soil; I -Aquifer I; II- Aquifer II and silicified breccia zone.

mainly Cu and Fe, and minor Zn, Pb, S, V and Os.

Based on the results, we conclude that finding of these metal-bearing nanoparticles in any medium is not just by chance, although single-crystal nanoparticles are extremely rare. Considering the variations in behaviors of nanoparticles in liquids and gases, a comparison of the nanoparticles in groundwater and ascending gas flow samples is emphasized in Table 7. Occurring as individual particles or particle aggregations, the metal-bearing nanoparticles with diverse crystalline characteristics present in both media. There is much variation with regard to the size and shape of the nanoparticles in groundwater in contrast to those carried by ascending gas flow, although these nanoparticles are with broadly similar elemental combinations. These gas-borne nanoparticles are characterized by a smaller and more homogeneous size, which enables them to be carried by ascending gas flow and to readily migrate upward (Cao et al., 2015; Luo et al., 2015). With respect to individual particles, those in groundwater have a wider range of shapes, such as irregular, rod-like, rounded, and ellipsoidal.

5.4. Origin, migration mechanism and prospecting significance of metal-bearing nanoparticles

Nanominerals are common and widely distributed in the atmosphere, seawater, groundwater and soil (Hochella et al., 2008). For example, abundant inorganic/organic nanoparticles with similar morphology are found in seawater from different locations and depths. These nanoparticles contain metals and may have played an important role in trace elements circulation in the oceans (Wells and Goldberg, 1991, 1992, 1994; Wells et al., 2000; Guo et al., 2000; Wu et al., 2001). By behaving differently from their coarser counterparts, nanoparticles from ore deposits are gaining research attention (Hochella et al., 2008; Reich et al., 2010, 2011; Hough et al., 2008, 2011, 2012). As reported in many studies, mineralization processes formed nanoparticles (Palenik et al., 2004; Deditius et al., 2011). Since minerals go through a nanophase stage during formation, they generate nanoparticles that retain in some cases (Hochella et al., 2002, 2008). It has been confirmed that various nanoparticles containing Au, Ag, Sb, Bi, Cu, Pb, Zn, Ti and Mg, can be directly observed in hypogene ores (Palenik et al., 2004; Reich et al., 2005, 2006; Deditius et al., 2011, 2018; Ciobanu et al., 2012; González-Jiménez et al., 2015; González-Jiménez and Reich, 2017).

In this study, amorphous nanoparticles, simple and complex poly-crystal nanoparticles are found in the background samples. These nanoparticles only contain common elements (e.g., O, Na, Ca, Si, Ti, Mg, Al and Cl), whereas ore-related elements (e.g., Pb, Zn, and Cu) are barely detected. This suggested that the Cu-, Zn-, Pb-, Fe-, As-, and S-bearing (some Ag-, Sb-, Bi-, and Sn-bearing) nanoparticles from the Kangjiawan deposit are most likely related to the concealed orebodies, which contain minerals of similar metal assemblages such as sphalerite,

galena, arsenopyrite, chalcopyrite, pyrrhotite, pyrite, silver sulfosalts and electrum (Zeng et al., 2000; Zhao et al., 2014). This is supported by the fact that the wall rocks contain low metal contents and man-made pollution (e.g., factory or refuse dump) is inexistent in the area. The discovery of metal-bearing nanoparticles must be a response to sampling sites that have orebodies underneath.

Based on the characteristics of nanoparticles, geological settings and hydrogeological settings of the deposit, these nanoparticles released from the deep-seated orebodies were likely generated at depth through post-mineralization fault activity and oxidation (Cao et al., 2010, 2015). Faults and breccias are well developed in the Kangjiawan deposit (Zeng et al., 2000; Zhang et al., 2007; Zuo et al., 2016). Faulting can mechanically grind the materials (e.g., ores and wall rocks) into nanoparticles. As previously documented, ore-related nanoparticles released from the crushed ores can be detected in deep fault gouges, such as the S-bearing nanoparticles and various Au-, Cu-, Zn-, Pb-, Mo-bearing nanoparticles with crystal structure deformations or jagged edges (Cao et al., 2010, 2015; Hu et al., 2015; Mi et al., 2017). Meanwhile, physicochemical (e.g., pressure and temperature) fluctuations led by faulting could generate chemical reactions of nearby minerals (Cao et al., 2015; Li et al., 2016). Besides, oxygen percolated through the well-developed fissures and breccias could oxidize the primary sulfide minerals in the deep-seated orebodies (Cao et al., 2010, 2015; Hu et al., 2015; Li et al., 2016). The ore-related nanoparticles identified in this study mainly exist as oxides and sulfates, suggesting that they may have been oxidation products from the deep-seated orebodies.

Metals may be transferred from the orebodies upwards and/or laterally through transported covers (Anand et al., 2016). Apart from an ionic form, ore-forming elements can also be transported in a nanoparticle form. As previously documented, metal-bearing nanoparticles can be transported in groundwater (Li et al., 2016; Cheng et al., 2018) and carried upwards by ascending gas flow and microbubbles (Etiope, 1998; Malmqvist et al., 1999; Cao et al., 2009a, 2010; Dai et al., 2015; Luo et al., 2015; Wang et al., 2016; Li et al., 2017). Some of these metal-bearing nanoparticles would be adsorbed on clay minerals (e.g., kaolinite and halloysite), or appear in vegetation and invertebrate tissues (Cao et al., 2010; Lintern et al., 2013; Hu et al., 2017, 2018).

Based on the geological characteristics of the Kangjiawan deposit and the discussion above, a schematic genetic model of the metal-bearing nanoparticles is shown in Fig. 9. Characterizing the morphological features and chemical compositions of nanoparticles via TEM is a new and potentially useful prospecting method for deep-seated orebodies. Present in different media (e.g., groundwater, ascending gas flow and soil) around the deposit, metal-bearing nanoparticles are closely genetically linked to the deep-seated orebodies. In this paper, we firstly propose that ore-forming elements could exist and migrate in the form of amorphous nanoparticles, single-crystal nanoparticles, poly-

crystal nanoparticles and complex polycrystal nanoparticles. Therefore, the forms of migration of the ore-forming elements can be enriched, which aids in explaining geochemical anomalies. Furthermore, many amorphous nanoparticles in different media can efficiently transfer ore-forming elements.

Acknowledgments

References

Aina, A., Olorunfemi, M.O., 1996. Comparative field results for electrical resistivity, magnetic, gravity and LVF methods over a marble lens. Explor. Geophys. 27 (4), 217–222.

Anand, R.R., Cornelius, M., Phang, C., 2007. Use of vegetation and soil in mineral exploration in areas of transported overburden, Yilgarn Craton, Western Australia: a contribution towards understanding metal transportation processes. Geochem. Explor. Environ. Anal. 7 3, 267–288.

Anand, R.R., Aspandiar, M.F., Noble, R.R.P., 2016. A review of metal transfer mechanisms through transported cover with emphasis on the vadose zone within the Australian regolith. Ore Geol. Rev. 73, 394–416.

Antropova, L.V., Goldberg, I.S., Voroshilov, N.A., Ryss, J.S., 1992. New methods of regional exploration for blind mineralization: application in the USSR. J. Geochem. Explor. 43 (2), 157–166.

Butt, C.R.M., Gole, M.J., 1985. Helium in soil and overburden gas as an exploration pathfinder-an assessment. J. Geochem. Explor. 24 (2), 141–173.

Cameron, E.M., Hamilton, S.M., Leybourne, M.I., Hall, G.E.M., Mcclenaghan, M.B., 2004. Finding deeply buried deposits using geochemistry. Geochem. Explor. Environ. Anal. 4 (1), 7–32.

Cao, J.J., Hu, R.Z., Liang, Z.R., Peng, Z.L., 2009a. TEM observation of geogas-carried particles from the Changkeng concealed gold deposit, Guangdong Province, South China. J. Geochem. Explor. 101 (3), 247–253.

Cao, J.J., 2009b. A technique for detecting concealed deposits by combining geogas particle characteristics with element concentrations. Metal Mine. 392 (2), 1–4 (in Chinese with English abstract).

Cao, J.J., Hu, X.Y., Jiang, Z.T., Li, H.W., Zou, X.Z., 2010. Simulation of adsorption of gold nanoparticles carried by gas ascending from the Earth's interior in alluvial cover of the middle-lower reaches of the Yangtze River. Geofluids 10 (3), 438–446.

Cao, J.J., Li, Y.K., Jiang, T., Hu, G., 2015. Sulfur-bearing particles emitted by concealed sulfide ore deposits: an unknown source of sulfur-bearing particles in the atmosphere. Atmos. Chem. Phys. 15 (12), 6959–6969.

Cheng, S.T., Cao, J.J., Li, Y.K., Hu, G., Yi, Z.B., 2018. TEM observations of particles in groundwater and their prospecting significance in the Bofang copper deposit, Hunan, China. Ore Geol. Rev. 95, 382–400.

Ciobanu, C.L., Cook, N.J., Utsunomiya, S., Kogawa, M., Green, L., Gilbert, S., Wade, B., 2012. Gold-telluride nanoparticles revealed in arsenic-free pyrite. Am. Mineral. 97, 1515–1518.

Clark, R.J., Meier, A.L., Riddle, G., 1990. Enzyme leaching of surficial geochemical samples for detecting hydromorphic trace-element anomalies associated with precious-metal mineralized bedrock buried beneath glacial overburden in northern Minnesota. Gold 90, 189–207.

Consani, S., Carbone, C., Dinelli, E., Balić-Žunić, T., Cutroneo, L., Capello, M., Salviulo, G., Lucchetti, G., 2017. Metal transport and remobilisation in a basin affected by acid mine drainage: the role of ochreous amorphous precipitates. Environ. Sci. Pollut. Res. 24 (18), 15735–15747.

Craven, B., Rovira, T., Grammer, T., Styles, M., 2000. The role of geophysics in the discovery and delineation of the Cosmos Nickel Sulphide Deposit, Leinster area, Western Australia. Explor. Geophys. 31 (2), 201–209.

Dai, D.L., Cao, J.J., Lai, P.X., Wu, Z.Q., 2015. TEM study on particles transported by ascending gas flow in the Kaxiutata iron deposit, Inner Mongolia, North China. Geochem. Explor. Environ. Anal. 15 (4), 255–271.

Deditius, A.P., Utsunomiya, S., Reich, M., Kesler, S.E., Ewing, R.C., Hough, R., Walshe, J., 2011. Trace metal nanoparticles in pyrite. Ore Geol. Rev. 42, 32–46.

Deditius, A.P., Reich, M., Simon, A.C., Suvorova, A., Knipping, J., Roberts, M.P., Rubanov, S., Dodd, A., Saunders, M., 2018. Nanogeochemistry of hydrothermal magnetite. Contrib. Miner. Petrol. 173, 46.

Etiope, G., 1998. Transport of radioactive and toxic matter by gas microbubbles in the ground. J. Environ. Radioact. 40 (1), 11–13.

Gao, Y.Y., Wang, M.Q., Zhang, D.E., 2011. Application of 'metals-in-soil-gas' techniques to mineral exploration in exotic overburden. Geochem. Explor. Environ. Anal. 11 (2), 63–70.

Geffen, P.W.G.V., Kyser, T.K., Oates, C.J., Ihlenfeld, C., 2012. Till and vegetation geochemistry at the Talbot VMS Cu-Zn prospect, Manitoba, Canada: implications for mineral exploration. Geochem. Explor. Environ. Anal. 12 (1), 67–88.

Ghavami-Riabi, R., Theart, H.F.J., Jager, C.D., 2008. Detection of concealed Cu-Zn massive sulfide mineralization below eolian sand and a calcrete cover in the eastern part of the Namaqua Metamorphic Province, South Africa. J. Geochem. Explor. 97 (2–3), 83–101.

González-Jiménez, J.M., Reich, M., Camprubí, A., Gervilla, F., Griffin, W.L., Colás, V., O'Reilly, S.Y., Proenza, J.A., Pearson, N.J., Centeno-García, E., 2015. Thermal metamorphism of mantle chromites and the stability of noble-metal nanoparticles. Contrib. Miner. Petrol. 170, 15.

González-Jiménez, J.M., Reich, M., 2017. An overview of the platinum-group element nanoparticles in mantle-hosted chromite deposits. Ore Geol. Rev. 81, 1236–1248.

Gray, D.J., Noble, R.R.P., Reid, N., Sutton, G.J., Pirlo, M.C., 2016. Regional scale hydrogeochemical mapping of the northern Yilgarn Craton, Western Australia: a new technology for exploration in arid Australia. Geochem. Explor. Environ. Anal. 16 (1), 100–115.

Guo, L.D., Santschi, P.H., Warnken, K.W., 2000. Trace metal composition of colloidal organic material in marine environments. Mar. Chem. 70, 257–275.

Hochella Jr., M.F., 2002. There's plenty of room at the bottom: nanoscience in geochemistry. Geochim. Cosmochim. Acta 66, 735–743.

Hochella Jr., M.F., Lower, S.K., Maurice, P.A., Penn, R.L., Sahai, N., Sparks, D.L., Twining, B.S., 2008. Nanominerals, mineral nanoparticles, and Earth systems. Science 319, 1631–1635.

Hough, R.M., Noble, R.R.P., Hitchen, G.J., Hart, R., Reddy, S.M., Saunders, M., Clode, P., Vaughan, D., Lowe, J., Gray, D.J., Anand, R.R., Butt, C.R.M., Verrall, M., 2008. Naturally occurring gold nanoparticles and nanoplates. Geology 36, 571–574.

Hough, R.M., Noble, R.R.P., Reich, M., 2011. Natural gold nanoparticles. Ore Geol. Rev. 42, 55–61.

Hough, R.M., Reich, M., Noble, R., 2012. Noble metal nanoparticles in ore systems. In: Barnard, Amanda S., Guo, Haibo (Eds.), Nature's Nanostructures. Pan Stanford Publishing Pte. Ltd. (Hardcover) 141-167-Book Chapter.

Hu, G., Cao, J.J., Lai, P.X., Hopke, P.K., Holub, R.F., Zeng, J.N., Wang, Z.H., Wu, Z.Q., 2015. Characteristics and geological significance of particles on fractures from the Dongshengmiao polymetallic pyrite deposit, Inner Mongolia, China. Geochem. Explor. Environ. Anal. 15 (4), 373–381.

Hu, G., Cao, J.J., Jiang, T., Wang, Z.Y., Yi, Z.B., 2017. Prospecting application of nanoparticles and nearly nanoscale particles within plant tissues. Resour. Geol. 67 (3), 316–329.

Hu, G., Cao, J.J., Jiang, T., 2018. Discovery and prospecting significance of metal-bearing nanoparticles within natural invertebrate tissues. Ore Geol. Rev. 99, 151–165.

Huang, J.C., Peng, J.T., Yang, J.H., Zhang, B.L., Xu, C.X., 2015. Precise zircon U-Pb and molybdenite Re-Os dating of the Shuikoushan granodiorite-related Pb-Zn mineralization, southern Hunan, South China. Ore Geol. Rev. 71, 305–317.

Kelley, D.L., Hall, G.E.M., Closs, L.G., Hamilton, I.C., McEwen, R.M., 2003. The use of partial extraction geochemistry for copper exploration in northern Chile. Geochem. Explor. Environ. Anal. 3 (1), 85–104.

Konrad-Schmolke, M., Halama, R., Wirth, R., Thomen, A., Klitscher, N., Morales, L., Schreiber, A., Wilke, F.D.H., 2018. Mineral dissolution and reprecipitation mediated by an amorphous phase. Nat. Commun. 9, 1637.

Koplus, A.V., Puzanov, L.S., Zubov, M.A., Tumanyan, N.Z., 2009. Primary multiplicative halos of concealed fluorite mineralization. Int. Geol. Rev. 16 (12), 1322–1332.

Kristiansson, K., Malmqvist, L., 1982. Evidence for non-diffusive transport of 222/86 Rn in the ground and a new physical model for the transport. Geophysics 47 (10), 1444–1452.

Leybourne, M.I., Cameron, E.M., 2010. Groundwater in geochemical exploration. Geochem. Explor. Environ. Anal. 10 (2), 99–118.

Li, Y.K., Cao, J.J., Hopke, P.K., Holub, R.F., Jiang, T., 2016. The discovery of the metallic particles of groundwater from the Dongshengmiao polymetallic deposit, Inner Mongolia, and their prospecting significance. J. Geochem. Explor. 161, 49–61.

Li, D.W., Cao, J.J., Ke, H.L., Liu, C., Wei, X.J., 2017. Study of particles from the Kafang copper deposit in Gejiu city, Yunnan. Geochem. Explor. Environ. Anal. 17 (4), 367–377.

Lintern, M., Anand, R., Ryan, C., Paterson, D., 2013. Natural gold particles in Eucalyptus leaves and their relevance to exploration for buried gold deposits. Nat. Commun. 4, 2274.

Lintern, M.J., Anand, R.R., 2017. Dispersion of gold and other metals by trees, gravels and soils near Boddington Gold Deposit, Western Australia. J. Geochem. Explor. 181, 10–21.

Luo, X.R., Li, J.B., Wu, H., Zhang, P.H., 1999. A survey of ionic conductivity of soil and its significance in prospecting for ore deposits concealed under thick overburden. J. Geochem. Explor. 66 (1–2), 307–311.

Luo, S.Y., Cao, J.J., Yan, H.B., Yi, J., 2015. TEM observations of particles based on sampling in gas and soil at the Dongshengmiao polymetallic pyrite deposit, Inner Mongolia, Northern China. J. Geochem. Explor. 158, 95–111.

Malmqvist, L., Kristiansson, K., 1985. A physical mechanism for the release of free gases in the lithosphere. Geoexploration 23 (4), 447–453.

Malmqvist, L., Kristiansson, K., Kristiansson, P., 1999. Geogas prospecting-An ideal industrial application of PIXE. Nucl. Instrum. Methods Phys. Res. 150 (1–4), 484–490.

Mann, A.W., Birrell, R.D., Mann, A.T., Humphreys, D.B., Perdrix, J.L., 1998. Application of the mobile metal ion technique to routine geochemical exploration. J. Geochem. Explor. 61 (1–3), 87–102.

Mi, Y.B., Cao, J.J., Wu, Z.Q., Wang, Z.H., 2017. Transmission electron microscopy analysis on fault gouges from the depths of the Bairendaba polymetallic deposit, Inner Mongolia, China. J. Nanosci. Nanotechnol. 17 (9), 6549–6557.

Mohanty, W.K., Mandal, A., Sharma, S.P., Gupta, S., Misra, S., 2011. Integrated geological and geophysical studies for delineation of chromite deposits: a case study from Tangarparha, Orissa, India. Geophysics 76 (5), B173–B185.

No. 217 Team, Hunan Bureau of Nonferrous Metals Geoexploration. 1982. The assessment report of the Kangjiawan lead-zinc ore district from the Shuikoushan orefield (in Chinese).

Noble, R.R.P., Lintern, M.J., Townley, B., Anand, R.R., Gray, D.G., Reid, N., 2013. Metal migration at the North Miitel Ni sulphide deposit in the southern Yilgarn Craton: Part 3, gas and overview. Geochem. Explor. Environ. Anal. 13 (2), 99–113.

Palenik, C.S., Utsunomiya, S., Reich, M., Kesler, S.E., Wang, L., Ewing, R.C., 2004. "Invisible" gold revealed: Direct imaging of gold nanoparticles in a Carlin-type deposit. Am. Mineral. 89, 1359–1366.

Park, J.Y., Jeon, S.H., Kim, J.N., Chon, H.T., 2014. A biogeochemical orientation study in Mo skarn deposits, Jecheon district in Korea. J. Geochem. Explor. 146, 9–16.

Pouget, E.M., Bomans, P.H., Dey, A., Frederik, P.M., De, W.G., Sommerdijk, N.A., 2010. The development of morphology and structure in hexagonal vaterite. J. Am. Chem. Soc. 132 (33), 11560–11565.

Reich, M., Kesler, S.E., Utsunomiya, S., Palenik, C.S., Chryssoulis, S.L., Ewing, R.C., 2005. Solubility of gold in arsenian pyrite. Geochim. Cosmochim. Acta 69, 2781–2796.

Reich, M., Utsunomiya, S., Kesler, S.E., Wang, L., Ewing, R.C., Becker, U., 2006. Thermal behavior of metal nanoparticles in geologic materials. Geology 34, 1033.

Reich, M., Chryssoulis, S.L., Deditius, A., Palacios, C., Zúñiga, A., Weldt, M., Alvear, M., 2010. "Invisible" silver and gold in supergene digenite (Cu1.8S). Geochim. Cosmochim. Acta 74, 6157–6173.

Reich, M., Hough, R.M., Deditius, A., Utsunomiya, S., Ciobanu, C.L., Cook, N.J., 2011. Nanogeoscience in ore systems research: principles, methods, and applications: Introduction and preface to the special issue. Ore Geol. Rev. 42, 1–5.

Roberts, D.E., Hudson, G.R.T., 1983. The Olympic Dam copper-uranium-gold deposit, Roxby Downs, South Australia. Econ. Geol. 78 (5), 799–822.

Tong, C.H., Li, J.C., Ge, L.Q., Yang, F.G., 1998. Experimental observation of the nanoscale particles in geogas matters and its geological significance. Sci. China Ser. D 41 (3), 325–329.

Varentsov, I.M., Kulikov, V.A., Yakovlev, A.G., Yakovlev, D.V., 2013. Possibilities of magnetotelluric methods in geophysical exploration for ore minerals. Izv. Phys. Solid Earth 49 (3), 309–328.

Wan, W., Wang, M.Q., Hu, M.Y., Gao, Y.Y., 2017. Identification of metal sources in Geogas from the Wangjiazhuang copper deposit, Shandong, China: evidence from lead isotopes. J. Geochem. Explor. 172, 167–173.

Wang, M.Q., Gao, Y.Y., Liu, Y.H., 2008. Progress in the collection of Geogas in China. Geochem. Explor. Environ. Anal. 8 (2), 183–190.

Wang, X.Q., Cheng, Z.Z., Lu, Y.X., Xu, L., Xie, X.J., 1997. Nanoscale metals in Earthgas and mobile forms of metals in overburden in wide-spaced regional exploration for giant deposits in overburden terrains. J. Geochem. Explor. 58 (1), 63–72.

Wang, Z.Y., Cao, J.J., Lin, Z.X., Wu, Z.Q., 2016. Detailed information about soil particles in the Xiaohulishan deposit, Inner Mongolia, China. J. Geochem. Explor. 169, 30–42.

Wei, X.J., Cao, J.J., Holub, R.F., Hopke, P.K., Zhao, S.J., 2013. TEM study of geogas-transported nanoparticles from the Fankou lead-zinc deposit, Guangdong Province, South China. J. Geochem. Explor. 128, 124–135.

Wells, M.L., Goldberg, E.D., 1991. Occurrence of small colloids in sea water. Nature 353, 342–344.

Wells, M.L., Goldberg, E.D., 1992. Marine submicron particles. Mar. Chem. 40, 5–18.

Wells, M.L., Goldberg, E.D., 1994. The distribution of colloids in the North Atlantic and Southern Oceans. Limnol. Oceanogr. 39, 286–302.

Wells, M.L., Smith, G.J., Bruland, K.W., 2000. The distribution of colloidal and particulate bioactive metals in Narragansett Bay, RI. Mar. Chem. 71, 143–163.

Williams, T.M., Gunn, A.G., 2002. Application of enzyme leach soil analysis for epithermal gold exploration in the Andes of Ecuador. Appl. Geochem. 17 (4), 367–385.

Wu, J., Boyle, E., Sunda, W., Wen, L.S., 2001. Soluble and colloidal iron in the oligotrophic north atlantic and north pacific. Science 293 (5531), 847–849.

Xu, D.R., Liu, J., Chen, G.H., 2002. Petrochemical characters of silicified breccia in the Kangjiawan deposit, Changning, Hunan. Chin. J. Geol. 37 (3), 356–364 (in Chinese with English abstract).

Yang, C.Y., 1985. The discovery and genesis of the Kangjiawan Pb-Zn deposit: Geology and Prospecting. 21(5), 1–7 (in Chinese).

Yang, J.H., Peng, J.T., Zheng, Y.F., Hu, R.Z., Bi, X.W., Zhao, J.H., Huang, J.C., Zhang, B.L., 2016. Petrogenesis of the Mesozoic Shuikoushan Seraluminous I-type granodioritic intrusion in Hunan province, South China: middle-lower crustal reworking in an extensional tectonic setting. J. Asian Earth Sci. 123, 224–242.

Yilmaz, H., Sonmez, F.N., Carranza, E.J.M., 2015. Discovery of Au-Ag mineralization by stream sediment and soil geochemical exploration in metamorphic terrain in western Turkey. J. Geochem. Explor. 158, 55–73.

Zeng, N.S., Izawa, E., Motomura, Y., Lai, L.R., 2000. Silver minerals and paragenesis in the Kangjiawan Pb-Zn-Ag-Au deposite of the Shuikoushan mineral district, Hunan province, China. Can. Mineral. 38 (1), 11–22.

Zhang, Y.H., Lin, G., Roberts, P., Ord, A., 2007. Numerical modelling of deformation and fluid flow in the Shuikoushan district, Hunan Province, South China. Ore Geol. Rev. 31 (1–4), 261–278.

Zhao, Z.X., Xu, Z.W., Zuo, C.H., Lu, J.J., Lu, R., 2014. Fluid inclusion and stable isotope studies on Kangjiawan Pb-Zn-Au-Ag deposit, Hunan Province, South China. Acta Geologica Sinica (English Edition) 82 (2), 1216–1217.

Zhou, S.C., Liu, X.H., Tong, C.H., Hu, B., 2014. Application research of geogas survey in prospecting concealed ore. Acta Geol. Sin. 88 (4), 736–754 (in Chinese with English abstract).

Zuo, C.H., Xu, Z.W., Lu, X.C., Zhao, Z.X., Chen, W., Wang, H., Lu, J.J., 2014. Petrogenesis of the Late Jurassic Laomengshan rhyodacite (Southeast China): constraints from zircon U-Pb dating, geochemistry and Sr-Nd-Pb-Hf isotopes. Int. Geol. Rev. 52 (16), 1964–1983.

Zuo, C.H., Qu, J.B., Zuo, Z.Y., Zuo, Z., Li, D.P., 2016. Genesis of breccia and its relationship with mineralization in the Kangjiawan lead-zinc deposit of Changning County, Hunan Province. Geol. Explor. 52 (2), 251–260 (in Chinese with English abstract).